

## Examination of the forces controlling dust dispersion by shock waves

O. J. Ugarte, R. W. Houim, and E. S. Oran\*

*University of Maryland, College Park, Maryland 20740, USA*

(Received 22 March 2017; published 28 July 2017)

The interaction between a shock wave and a thin layer of inert dust is studied by solving unsteady, multidimensional Navier-Stokes equations representing the interactions between a compressible gas and incompressible particles. The system studied consists of a layer of densely packed limestone dust containing particles of uniform diameter ( $40\ \mu\text{m}$ ) that interact with a shock of strength  $M_s = 1.4$ . Particle dispersion is investigated by comparing vertical particle accelerations due to Archimedes, gravitational, intergranular, and aerodynamic drag and lift forces. The simulations show that the shock produces two dust regions: a compacted layer and a dispersed region. The layer compaction, which increases the intergranular particle stress, is produced by drag and Archimedes forces. The dispersed dust is produced by forces that change in time as the shock passes. Initially, the dispersion is caused by intergranular forces. Later it is driven by a tradeoff between lift and drag forces. Eventually, drag forces dominate. Comparisons of the computations to experimental shock-tube data reproduced the observed initial growth of the dispersed dust and later leveled off. Particle agglomeration in the experiments made it difficult to determine a true particle size experimentally, although the computations for  $40\text{-}\mu\text{m}$  particles explain the experimental data.

DOI: [10.1103/PhysRevFluids.2.074304](https://doi.org/10.1103/PhysRevFluids.2.074304)

### I. INTRODUCTION

The interaction between high-speed flows and dust particles occurs naturally, as in tornadoes, volcanoes, and dust storms, and in industrial activities such as coal mining, food processing, and grain storage. This interaction becomes critical when the system involves reactive dust material, such as coal, sawdust, grain, and even some powdered metals. For example, the damage produced by explosions in a mineshaft can be enhanced or mitigated by the specific interaction of dust particles with a shock wave [1]. This interaction, however, is far from being well understood, as it depends strongly on the particular materials involved, the geometry of the interaction, and is a complex multiphase flow that involves a wide range of temporal and spatial scales.

Even though there are many complex processes occurring when shocks interact with particles, it has been possible to determine some of the basic, global features of the shock-dust interaction through the study of simple configurations. For example, we know that when a shock wave interacts with a dust layer settled on the surface of a channel, a situation resembling that in a coal mine explosion, the shock disperses dust particles behind the shock front [2–4]. If the dust itself is a reactive material, the dispersed particles in the shocked-heated gas can begin to react and release energy, thus strengthening the shock wave which in turn intensifies the dust dispersion. The result is a positive feedback between the shock dispersion and energy release that can lead to a secondary gas-dust explosion [5,6].

The purpose of this paper is to provide a detailed, quantitative study of the physical processes responsible for dispersing dust particles behind a moving shock. The vehicle for this study is an unsteady, multidimensional numerical solution of two coupled sets of Navier-Stokes equations, one for the gas and one for the particles [7]. The set of fluid equations for the solid particles is derived from kinetic theory of granular flow [8] and is valid for dilute to dense particle concentrations (that

---

\*Corresponding author: eoran@umd.edu

TABLE I. Forces acting on particles, as determined from Eqs. (5) and (13) in the text.

Drag	$K_{sg}(\mathbf{v}_g - \mathbf{v}_s)$	Results from relative motion between gas and particles. It acts along the direction of $(\mathbf{v}_g - \mathbf{v}_s)$ .
Lift	$C_l \alpha_s \rho_g (\mathbf{v}_s - \mathbf{v}_g) \times (\nabla \times \mathbf{v}_g)$	Results from gas-phase shear, acting perpendicularly to $(\mathbf{v}_g - \mathbf{v}_s)$ .
Archimedes Force	$-\alpha_s \nabla p_g$	Results from gas-phase pressure forces pushing on the particles.
Intergranular Stress	$\nabla p_s + \nabla p_{\text{fric}}$	Resulting from particle collisions and frictional stress, the latter for high particle concentrations.
Gravitational	$\alpha_s \rho_s \mathbf{g}$	Weight per unit volume of the particles.

is, from  $\alpha_s < 0.01\%$  up to  $\alpha_s = 64\%$ , where  $\alpha_s$  is the solid volume fraction). These sets of equations are coupled by terms describing the interactions of the gas and the particles, and the entire set of equations is solved by a high-order numerical method. Details of the model and its solution are summarized in Sec. III and discussed in detail in Ref. [7].

In order to study the mechanisms controlling the dispersion of dust produced by a shock wave, we evaluate the different forces acting on the particles as the shock moves through them. These forces are the aerodynamics lift and drag forces, which result from the velocity difference between the particles and the gas; buoyancy, which might be small at the initial stages; particle-particle interactions, which cause collisional and frictional stress; and the force produced by gas pressure gradients on particles, which is sometimes called the Archimedes force. (The relevant forces are discussed in more detail in Sec. III and listed in Table I.) The specific problem and geometry studied here is shown schematically in Fig. 1.

Before describing the results of specific calculations and the resulting forces, it is important to discuss relevant prior work on shock-dust interactions and, in particular, the origins of some of the controversies that have arisen. The brief historical discussion presented in the next section shows some of the complexities encountered when analyzing shock-dust systems.

## II. BACKGROUND AND CONTROVERSIES

Here we view the interaction of particles with a shock wave as a two-stage process. The first stage is produced immediately after the shock and dust come into contact and the dust begins to rise. The second stage occurs at a longer time and length scale, where the evolution of the initial dust rising is controlled by the conditions in the shocked region. The initial stage, that is, immediately behind the shock, is related to an interesting controversy created by two relatively early sets of shock-tube experiments.

In the first of these experiments, Gerrard [2] varied the Mach number  $M_s$  and height  $h_d$  of the dust layer in the ranges  $1.2 < M_s < 1.6$  and  $0.10 \text{ cm} < h_d < 0.27 \text{ cm}$ , respectively, and considered dust types with properties similar to dry sand and blackboard chalk. The first important observation from

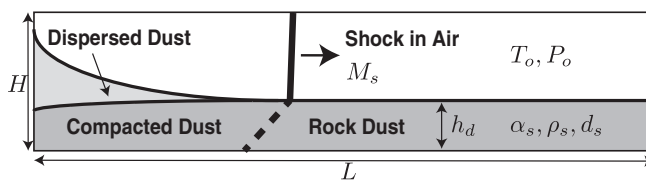


FIG. 1. Schematic of shock wave propagating on top of and through a dust layer in a channel of height  $H$  and length  $L$ . Dust layer is characterized by layer thickness  $h_d$ , particle volume fraction  $\alpha_s$ , particle density  $\rho_s$ , and particle diameter  $d_s$ . The unperturbed gas is defined by  $T_o$  and  $P_o$ . Incident shock Mach number is  $M_s$  (see Table II for values).

these experiments was related to the structure of the shock wave, which curved as it entered the dust layer. The second important observation was that after the shock passes over the dust layer, there is a delay in the dust lifting that depends on  $h_d$ , among other factors. Based on these observations, Gerrard concluded that the lifting delay was the result of shock deflection *in* the dust layer. In particular, it was proposed that once the shock enters the dust, it turns and propagates towards the bottom of the dust layer. Then, after reaching the bottom of the dust layer, it reflects back and propels particles upwards.

This explanation was challenged years later by Fletcher [9], who did similar experiments. As a result of the new experiments, he attributed the particle lift to the strong flow field generated behind the shock wave. He supported this interpretation by calculating the location where a deflected pressure wave would have returned to the surface after reflecting from the bottom of the dust layer, and then looking for dust lifting at this location. Neither his work nor the earlier work by Gerrard indicated any substantial disturbance at this calculated location.

The differing observations of Gerrard and Fletcher have been clarified by recent numerical simulations. Namely, Houim *et al.* [10] showed that particle lifting behind a moving shock depends on particle-gas and particle-particle interactions occurring above and inside the dust layer, respectively. In particular, particle lifting is initially driven by the high hydrodynamic shear produced above the dust layer, whereas gas flowing through the dust layer compacts particles in the dust. The compaction of the dust, in turn, evolves to a compaction wave that creates an upward force on the particles located at the dust surface after reflecting off of the channel floor. This force not only enhances the initial lifting process but also induces hydrodynamic instabilities on the dispersed particles.

Other controversies also arose because of the wide range of temporal and spatial scales characterizing shock-dust interactions, all of which work together to complicate the problem. As an example, consider the effect of particle size on the height of particle lifting. One phenomenon observed is a boundary layer, comprised of dust and gas, forming on top of the dust layer just behind the shock wave. An early theory developed by Hwang [11] evaluated the effects of lift and drag forces on particles to explain how particles rise in this boundary layer. The analysis was restricted to weak shocks ( $M_s < 1.44$ ) in the laminar region behind the shock wave, before any turbulence develops. Hwang concluded that larger particles are lifted higher than smaller particles, and that particle dispersion is enhanced by stronger shock waves.

In addition, Hwang predicted that there would be a delay in the lifting process and that this delay increases for larger particles. The computations examined a range of particle diameters from  $1\ \mu\text{m}$  to  $200\ \mu\text{m}$ . One result was that particles with a  $200\text{-}\mu\text{m}$  diameter were lifted twice as high as those particles with a  $5\text{-}\mu\text{m}$  diameter after approximately 1 ms, although  $1\text{-}\mu\text{m}$  particles were lifted higher in the first 0.6 ms. He included shock-tube results presented in Refs. [2,9] as well as his own experimental work to support his analysis.

There is a contradiction here with the earlier experiments by Suzuki and Adachi [12], which showed that smaller particles ( $84\ \mu\text{m}$ ) rise higher than larger ones ( $300\ \mu\text{m}$ ) within the first 40 cm behind the shock front. These apparently opposite conclusions arose because the authors made their observations on different length scales. Specifically, the process of particle lifting takes longer for larger particles, so the lifting delay process was still ongoing for  $300\text{-}\mu\text{m}$  particles within the 40-cm distance analyzed by Suzuki and Adachi. Therefore, although the experimental results were accurate in both cases, the conclusions were based on observations at different spatial and temporal scales.

The height that the dust cloud can reach behind a moving shock is an important parameter that affects dust concentration and, if the particles can react exothermically, the possibility of reaching explosive conditions. Chowdhury *et al.* [4] observed two regimes for the growth rate of the dust-cloud height ( $Y$ ) in shock tubes: a faster growth rate, where  $Y$  increases near linearly in time at the beginning of the process, and a slower growth rate of  $Y$  at later times. These experiments considered shock Mach numbers in the range  $1.1 < M_s < 1.6$ . The linear regime showed only a small variation in the slope of  $Y$  when two different thicknesses of dust layer were used,  $h_d = 3.2\ \text{mm}$  and  $h_d = 12.7\ \text{mm}$ . Moreover, the results in this work showed a delay in the transition from linear to the slow regime

for the thicker layer (12.7 mm). This delay was accompanied by intense fluctuations in the particle concentration above the dust surface.

The effect of dust-layer thickness ( $h_d$ ) on the dispersion of particles was studied for much thinner layers by Klemens *et al.* [3]. In their experiments, shock waves moving at velocities in the range 450–518 m/s interacted with dust layers with  $h_d = 0.1, 0.4,$  and  $0.8$  mm. The growth of the dispersed dust was quantified by calculating the time needed for the dust to rise 8 mm above the initial layer. Their results showed that particles in thinner layers take longer to reach this height. The experiments included two types of particles, silicon ( $\rho_s = 2340$  kg/m<sup>3</sup>) and coal ( $\rho_s = 1340$  kg/m<sup>3</sup>). They observed that the vertical velocity of the silicon particles showed larger variations when the height of the dust layer was increased. Why this occurs was not explained.

Many of the questions and issues about the behavior of shock-dust interactions can now, in principle, be addressed by numerical simulations. There are, however, many challenges and decisions required to construct a model that can do this. These involve determining models for the dust, that is, whether this granular material will be treated as particles or as fluid, ensuring that all of the relevant physical processes are appropriately included and, perhaps the most difficult, finding compressible algorithms that can accurately solve the equations for this multiphase flow. As an example, Fedorov and Fedorchenko [13] developed a method to solve a two-dimensional unsteady set of conservation equations for a mixture composed of gas and fine solid particles, and then they used this to model the interaction of shock waves with dust layers in laminar and turbulent regimes. Special care was taken to solve the equations, namely, multiple methods were used to ensure the accuracy of the solution. When the results were compared to experimental data [14], the pressure distribution obtained numerically and experimentally at selected locations in the shock tube showed good agreement. It should be noted, however, that the simulations considered more dilute dust-gas mixtures than the actual values in the experiments. Specifically, the particle concentrations in the computations were between two and ten times lower than the value considered in the experiments.

The subsequent work of Zydak and Klemens [15] studied the dust dispersion process behind a propagating shock wave by using an “Eulerian-Eulerian” approach, which means that the gas phase was modeled by the Navier-Stokes equations and the solid phase by a similar set of modified fluid equations. The objective was to develop a way to model dust dispersion and still use relatively large computational cells, thus lowering the cost of the computation and obtaining a model capable of describing large systems. This was achieved by injecting particles into the computational domain instead of modeling the initial dust rise. The vertical velocity at which the particles were injected into the computations was obtained from experimental results [3]. An important advance in the model was to include the Saffman and Magnus lift forces, as well as particle-particle collisions. The dust concentration in the dispersed region was obtained numerically and compared to experimental data from [3]. The comparison showed that the computations improved significantly when particle-particle collisions were included. On the contrary, little effect was noticed when Saffman or Magnus forces were implemented in the model.

Numerical simulations have been used to investigate how impulsive aspects of blast waves are modified when explosive charges contain metal particles. In particular, Balakrishnan *et al.* [16] used a three-dimensional, two-phase Eulerian-Lagrangian approach to calculate the momentum transfer between particles and gas in the explosion of a nitromethane charge that contained steel particles. Impulse features of this heterogeneous charge, such as pressure, velocity, and momentum flux distributions, were compared with those corresponding to a purely nitromethane explosive. The results indicated that adding particles significantly increased the impulse loading near the charge (within 4 times the diameter of the charge), but only a small increase was seen in the far field (about 20 times the diameters of the charge). The investigation indicated that the primary shock was insensitive to the size of the particles and that the total impulse was not modified by the particle size when particles were larger than 275  $\mu\text{m}$ . The study in Ref. [16] also analyzed the forces controlling the particle dynamics in the blast-particle interaction. Three forces were identified, namely, viscous drag, gas pressure gradient, and interparticle collisions. It was found that the three forces accelerate particles at a similar rate in the first 0.1 ms of the blast propagation. After this point, the effect of

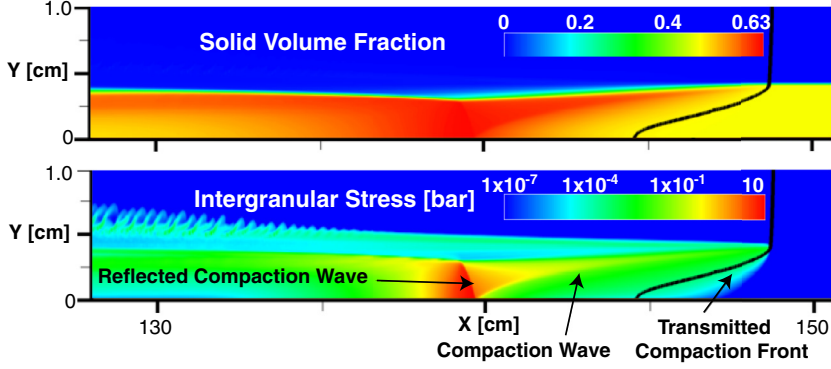


FIG. 2. Structure of shock particle behind a shock wave [10].

particle collisions weakens and the particle motion is controlled by viscous drag and gas pressure, although the acceleration produced by these two forces are reduced 3 and 6 orders of magnitude, respectively.

The next sections of this paper analyze unsteady, multidimensional numerical simulations of shock interactions with a dust layer. The simulations were performed using the numerical model created by Houim and Oran [7]. This model consists of two sets of Navier-Stokes equations describing a compressible gas coupled to dust that is described as a granular fluid. The model has been tested for nonreacting [10] and reactive stages of the interaction of compressible gases and reactive particles [6,17]. In particular, the model predicts a distinctive structure of the shock-dust interaction [10]. This structure is shown in Fig. 2, where the contours correspond to a moving shock ( $M_s = 1.4$ ) interacting with a layer of dust initially settled on the floor. The initial thickness and particle concentration of the dust layer are  $h_d = 0.32$  cm and  $\alpha_s = 0.47$ , respectively. The results in Ref. [10] showed that drag and pressure forces produce the compaction of the dust layer behind the shock. The front of the compacted dust evolves to a compaction wave through particle-particle collisions and frictional forces. The compaction wave reflects from the channel floor and reaches the dust surface, exerting an upward force on the particles and producing acoustic waves. The compaction front and compaction wave are marked in Fig. 2.

### III. METHODOLOGY

#### A. Governing equations

A full description of the numerical model used in this paper has been presented in Houim and Oran [7]. The physical model is based on the coupled set of compressible gas and granular-fluid equations. It should be noticed that even though the granular phase is incompressible, the gas-particle mixture as a whole is a compressible flow, and it is described by a hyperbolic system of equations [7]. A summary of the formulation is presented below for the case of nonreactive gas and dust materials.

The set of governing equations for the gas phase is

$$\frac{\partial \alpha_g \rho_g}{\partial t} + \nabla \cdot \alpha_g \rho_g \mathbf{v}_g = 0, \quad (1)$$

$$\frac{\partial \alpha_g \rho_g \mathbf{v}_g}{\partial t} + \nabla \cdot (\alpha_g \rho_g \mathbf{v}_g \mathbf{v}_g) = -\alpha_g \nabla p_g + \alpha_g \rho_g \mathbf{g} + \mathbf{S}^p, \quad (2)$$

$$\frac{\partial \alpha_g \rho_g E_g}{\partial t} + \nabla \cdot [\alpha_g \mathbf{v}_g (\rho_g E_g + p_g)] = -p_g \nabla \cdot (\alpha_s \mathbf{v}_s) + \alpha_g \rho_g \mathbf{g} \cdot \mathbf{v}_g + S_g^E, \quad (3)$$

and for the solid phase,

$$\frac{\partial \alpha_s \rho_s}{\partial t} + \nabla \cdot (\alpha_s \rho_s \mathbf{v}_s) = 0, \quad (4)$$

$$\frac{\partial \alpha_s \rho_s \mathbf{v}_s}{\partial t} + \nabla \cdot (\alpha_s \rho_s \mathbf{v}_s \mathbf{v}_s) + \nabla p_s + \nabla p_{\text{fric}} = -\alpha_s \nabla p_g + \alpha_s \rho_s \mathbf{g} - \mathbf{S}^p, \quad (5)$$

$$\frac{\partial \alpha_s \rho_s E_s}{\partial t} + \nabla \cdot (\alpha_s \rho_s E_s \mathbf{v}_s) = -p_s \nabla \cdot \mathbf{v}_s + S_s^{\text{PTE}}, \quad (6)$$

$$\frac{\partial \alpha_s \rho_s e_s}{\partial t} + \nabla \cdot (\alpha_s \rho_s e_s \mathbf{v}_s) = S_s^E. \quad (7)$$

The variables  $\rho$ ,  $p$ ,  $T$ ,  $\mathbf{v}$ , and  $\alpha$  represent density, pressure, temperature, velocity vector, and volume fraction. The subscript  $g$  refers to the gas phase and  $s$  to the particle phase.  $E_g$  is the total energy of the gas phase, and  $e_s$  is the solid internal energy. The ideal gas approximation is used to evaluate the gas-phase variables. The pseudothermal energy (PTE) of the granular phase, given by  $E_s$ , is a function of the granular temperature  $\Theta$ , which is a measure of the particle velocity fluctuations,

$$E_s = \frac{2}{3} \Theta. \quad (8)$$

The solid pressure  $p_s$  is determined by particle collisions. Based on kinetic theory,  $p_s$  is expressed as an equation of state for a granular gas [8],

$$p_s = \rho_s \Theta \{ \alpha_s [1 + 2(1 + e) \alpha_s g_0] \}, \quad (9)$$

where  $e$  is the coefficient of restitution and  $g_0$  is a radial distribution function, defined here in terms of the particle volume fraction  $\alpha_s$  and the random close-packing limit  $\alpha_{s,\text{max}}$  [8]:

$$\frac{1}{g_0} = 1 - \left( \frac{\alpha_s}{\alpha_{s,\text{max}}} \right)^{1/3}. \quad (10)$$

In this study,  $\alpha_{s,\text{max}}$  is equal to 0.65. If the particle volume fraction is large, it is necessary to account for the frictional-collisional pressure, which is produced by pressurelike forces from granular layers sliding over each other. Therefore, the total intergranular stress is given by

$$p_{s,\text{tot}} = p_s + p_{\text{fric}}, \quad (11)$$

where  $p_{\text{fric}}$  is obtained according to [18]

$$p_{\text{fric}} = \begin{cases} 0 & \text{if } \alpha_s < \alpha_{s,\text{crit}} \\ 0.1 \alpha_s \frac{(\alpha_s - \alpha_{s,\text{crit}})^2}{(\alpha_{s,\text{max}} - \alpha_s)^5} & \text{if } \alpha_s \geq \alpha_{s,\text{crit}}, \end{cases} \quad (12)$$

and  $\alpha_{s,\text{crit}} = 0.5$ . Given that the particle density  $\rho_s$  is assumed constant, the compressibility effect in the granular phase is produced through changes in the particle volume fraction.

The source term in the momentum equation,  $\mathbf{S}^p$ , couples the gas and particles through the drag and lift forces:

$$\mathbf{S}^p = -\mathbf{f}_{\text{drag}} - \mathbf{f}_{\text{lift}}. \quad (13)$$

In this equation, the drag force is given by [8]

$$\mathbf{f}_{\text{drag}} = K_{sg} (\mathbf{v}_g - \mathbf{v}_s), \quad (14)$$

where the coefficient  $K_{sg}$  is obtained from

$$K_{sg} = \begin{cases} 0.75 C_d \frac{\rho_g \alpha_g \alpha_s |\mathbf{v}_g - \mathbf{v}_s|}{d_s \alpha_s^{2.65}} & \text{if } \alpha_g \geq 0.8 \\ 150 \frac{\alpha_s^2 \mu_g}{\alpha_g d_s^2} - 1.75 \frac{\rho_g \alpha_s |\mathbf{v}_g - \mathbf{v}_s|}{d_s} & \text{if } \alpha_g < 0.8, \end{cases} \quad (15)$$

and  $d_s$  is the particle diameter. The drag coefficient  $C_d$  is defined as

$$C_d = \begin{cases} 24(\alpha_g \text{Re})^{-1} [1 + 0.15(\alpha_g \text{Re})^{0.687}] & \text{if } \alpha_g \text{Re} < 1000 \\ 0.44 & \text{if } \alpha_g \text{Re} \geq 1000, \end{cases} \quad (16)$$

which is a function of the Reynolds number,

$$\text{Re} = \frac{\rho_g |\mathbf{v}_g - \mathbf{v}_s| d_s}{\mu_g}. \quad (17)$$

In turn, the lift force is modeled by the Magnus lift force [19]

$$\mathbf{f}_{\text{lift}} = C_l \alpha_s \rho_g (\mathbf{v}_s - \mathbf{v}_g) \times (\nabla \times \mathbf{v}_g). \quad (18)$$

The source terms in the gas-phase energy, internal energy, and PTE equations of the solid phase are given by

$$S_g^E = -q_{\text{conv}} + \phi_{\text{visc}} - (\mathbf{f}_{\text{drag}} + \mathbf{f}_{\text{lift}}) \cdot \mathbf{v}_s - \phi_{\text{slip}}, \quad (19)$$

$$S_s^E = q_{\text{conv}} + \dot{\gamma}, \quad (20)$$

and

$$S_s^{\text{PTE}} = -\dot{\gamma} - \phi_{\text{visc}} + \phi_{\text{slip}}, \quad (21)$$

respectively. Here the convective heat flux between gas and particles is expressed as

$$q_{\text{conv}} = 6 \frac{\alpha_s \lambda_g \text{Nu}}{d_s^2} (T_g - T_s), \quad (22)$$

with the Nusselt number calculated from [20]

$$\text{Nu} = (7 - 10\alpha_s + 5\alpha_s^2)(1 + 0.7 \text{Re}^{0.2} \text{Pr}_g^{1/3}) + (1.33 - 2.4\alpha_s + 1.2\alpha_s^2) \text{Re}^{0.7} \text{Pr}_g^{1/3}. \quad (23)$$

The viscous damping of the PTE is given by [8]

$$\phi_{\text{visc}} = 3K_{sg} \Theta, \quad (24)$$

whereas the PTE production rate, resulting from the velocity slip between the gas and solid phases, is calculated according to [21]

$$\phi_{\text{slip}} = \frac{81\alpha_s \mu_g^2}{g_0 d_s^3 \rho_s \sqrt{\pi}} \frac{|\mathbf{v}_g - \mathbf{v}_s|^2}{\sqrt{\Theta}}. \quad (25)$$

The granular dissipation of PTE, resulting from inelastic particle collisions, is given by [22]

$$\dot{\gamma} = \frac{12(1 - e^2) g_0 \alpha_s^2 \rho_s \Theta^{3/2}}{\sqrt{\pi} d_s}. \quad (26)$$

The analysis presented below focuses on the forces responsible for the dispersion of particles in the postshock region. As seen in the granular momentum equation [Eq. (5) complemented by Eq. (13)], these forces arise from gravity, gas-particle interactions, and particle-particle interactions. A list of these forces is presented in Table I.

## B. Numerical solution method

The governing equations are solved numerically by an operator-splitting approach, which treats the hyperbolic and source terms separately. The solution algorithm uses a Godunov-based technique that is fifth-order-accurate in space and a third-order-accurate Runge-Kutta method for time advancement [23]. The gas-phase fluxes are computed by the HLLC Riemann solver, whereas the advection upstream splitting method is used to calculate the solid-phase fluxes. Grid resolution

TABLE II. Initial and geometrical conditions.

Channel height	$H$	10.8 cm
Channel length	$L$	324 cm
Initial dust-layer height	$h_d$	0.32 cm
Shock Mach number	$M_s$	1.4, 1.23, 1.6
Solid volume fraction	$\alpha_s$	0.47
Particle density	$\rho_s$	2500 kg/m <sup>3</sup>
Particle diameter	$d_s$	5, 20, 40, 80 $\mu\text{m}$
Undisturbed gas temperature	$T_o$	295 K
Undisturbed gas pressure	$P_o$	67 kPa

is achieved by adaptive mesh refinement using the PARAMESH library [24]. In this investigation, the computational grid uses seven levels of refinement, which set the minimum cell size to 94  $\mu\text{m}$ . Details of the computational algorithm are given in Ref. [7].

### C. Input parameters

Table II lists the channel dimensions and initial conditions of the system shown schematically in Fig. 1. These values are similar to those considered in the experiments performed in Refs. [4,25], whose data is used for validation of the model in Sec. V E. The left and right surfaces of the channel are nonreflecting, inflow-outflow boundary conditions, whereas the top and bottom surfaces are symmetry planes. The dust layer on the floor consists of uniform-sized particles with initial volume fraction  $\alpha_s = 0.47$ . In the base case of this investigation, the particle diameter is  $d_s = 40 \mu\text{m}$ . Additional particle diameters are considered later in the paper to compare the numerical results to experimental data.

The gas phase is modeled as air. The solid phase is modeled as limestone, with density, specific heat, and coefficient of restitution of  $\rho_s = 2500 \text{ kg/m}^3$ ,  $c_p = 987 \text{ J/kg K}$ , and  $e = 0.9$ , respectively. A shock wave traveling towards the right is placed 5 cm from the left boundary. Postshock conditions at the left side of the shock are determined from Rankine–Hugoniot relations. The background pressure in these calculations is 67 kPa, which was also chosen to match experimental conditions in Refs. [4,25].

## IV. BASE CASE: DUST RISING FOR 40- $\mu\text{m}$ LIMESTONE PARTICLES

### A. Dynamics of the gas and particles behind the shock wave

Figure 3 shows the solid volume fraction [Figs. 3(a)–3(c)], the magnitude of the difference of the gas and particle velocities [Fig. 3(d)], and the gas pressure [Fig. 3(e)] for particle diameter  $d_s = 40 \mu\text{m}$ ,  $M_s = 1.4$ , and conditions listed in Table II. Particle trajectories and gas streamlines are overlaid on the solid volume fraction in Figs. 3(b) and 3(c), respectively. The particle trajectories and gas streamlines are shown in the shock wave frame of reference.

In Fig. 3(a), the particle concentration shows two dust regions formed behind the moving shock: a dust layer, which has been compacted by the shock from the initial volume fraction  $\alpha_s = 0.47$  to values as high as  $\alpha_s = 0.6$ ; and a dispersed-dust region, composed of particles rising above the dust layer. The location of the shock front is shown in Fig. 3(a) by the isobar  $P = 67 \text{ kPa}$ . This isobar, however, only represents the shock front above the dust layer. Since the shock weakens as it propagates through the dust, it is not possible to define a gas-phase shock within the dust layer.

The particle trajectories in Fig. 3(b) indicate that particles, initially at rest, start moving immediately behind the shock. The motion of particles continues further behind the shock front, dispersing particles and compacting the dust layer. A detailed analysis of the forces controlling the particle motion behind the shock is given in the next sections.

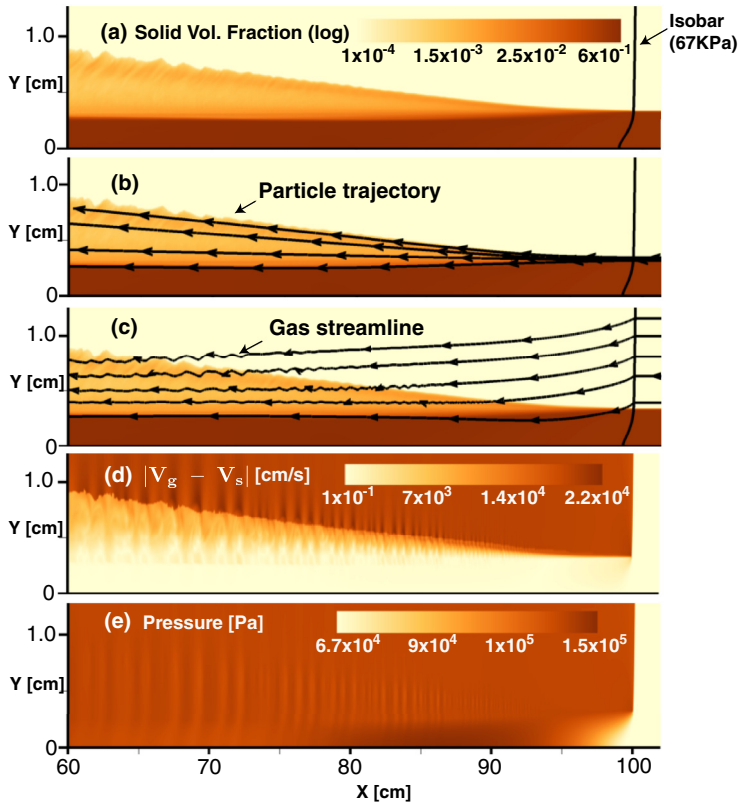


FIG. 3. Dust layer and dispersed dust forming behind a moving shock (a), with overlaid particle trajectories (b) and gas streamlines (c). Magnitude of the difference between the gas and particle velocities (d). Gas pressure field (e) shows a large gradient forming behind the shock inside the dust layer. Note that the vertical axis has been stretched approximately 10 times.

The gas streamlines in Fig. 3(c) show two interesting features. First, the gas flow deflects downwards at the shock front. The deflection of the flow continues behind the shock, especially between 85 cm and the shock location at 100 cm. Second, the gas flow oscillates above the dust layer. The onset of these oscillations varies with distance from the surface of the dust, starting at around 90 cm for the streamline located just above the dust layer.

Figure 3(d) shows the magnitude of the difference between the gas and particle velocities. The high velocity of the gas, produced by the moving shock, decreases as the gas interacts with the dust. Thus, the gas velocity is large near the edge of the dispersed-dust region, where the concentrations of particles are low, and decreases as the gas reaches regions with higher particle concentrations. Inside the dust layer, gas and particle motions are much weaker so that there is a negligible difference between their velocities.

The pressure field in Fig. 3(e) indicates a low-pressure region inside the dust layer between 95 and 100 cm, which results from the dissipation of the shock propagating through the dust. Following this low-pressure region, the pressure increases inside the dust layer between 80 cm and 93 cm. In the dispersed-dust region, the pressure field shows local variations which cause the flow oscillations seen in Fig. 3(c).

As seen in Fig. 3, the gas and particle dynamics vary according to the particle concentration and proximity to the shock front. In the next section, the particle dynamics is analyzed in the two regions forming behind the shock: the dispersed-dust region (Sec. IV B 1) and the dust layer (Sec. IV B 2).

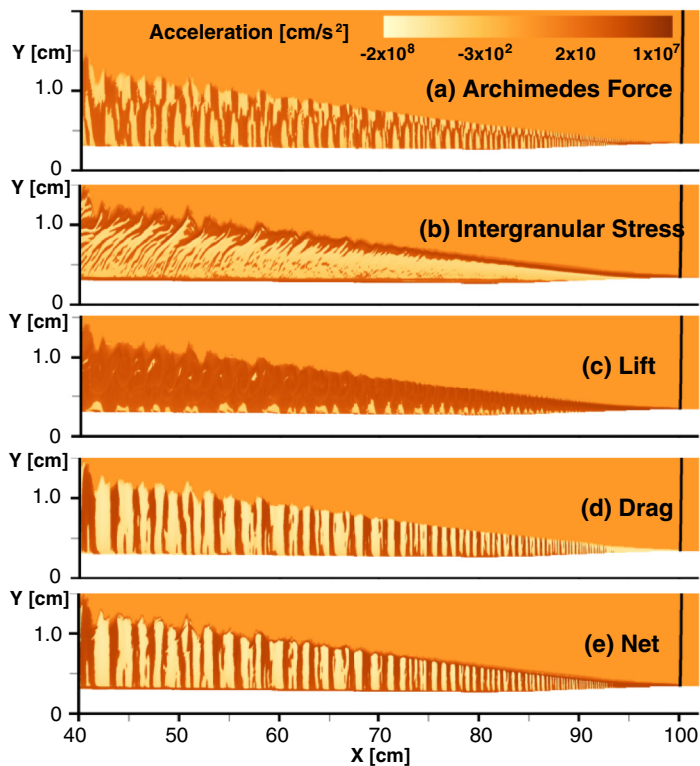


FIG. 4. Particle accelerations in the dispersed-dust region (defined as  $\alpha_{s,\text{disp}} < 0.1$ ), produced by the vertical component of the forces listed in Table I (except gravity). Forces have been normalized by  $\alpha_s \rho_s$ . Note that the vertical axis has been stretched approximately 10 times.

## B. Particle acceleration

Figures 4 and 5 show the vertical accelerations that the Archimedes force, intergranular stress, lift, and drag produce on particles (see Table I). The gravitational effect on particle acceleration ( $g = 9.81 \text{ m/s}^2$  in the entire domain) is much lower than the acceleration produced by the other forces and so is not presented in these results.

### 1. Particle acceleration in the dispersed dust

The dispersed-dust region is defined by the concentration of particles as  $\alpha_{s,\text{disp}} < 0.1$ . Figure 4 indicates that all of the forces produce positive and negative accelerations on the dispersed particles, except for the lift force, which accelerates particles upwards in almost the entire domain. The particle acceleration varies with distance from the shock. Specifically, intergranular and lift forces accelerate particles upwards in the first 5 cm behind the shock, which are opposed by drag. Within these first 5 cm behind the shock, the Archimedes force produces particle accelerations that alternate in upwards and downwards directions, although the upwards direction is predominant. All these forces are later modified by flow oscillations and by the dust-concentration gradients developing away from the shock front.

The Archimedes force is a function of the pressure gradient, namely,  $F_{\text{Arch}} = -\alpha_s \nabla p_g$ . For this reason, the particle acceleration produced by  $F_{\text{Arch}}$  in Fig. 4(a) is closely related to the pressure contour in Fig. 3(e). The Archimedes force accelerates particles upwards near the shock as a result of the high pressure produced at the surface of the dust layer. Further behind the shock,  $F_{\text{Arch}}$  produces positive and negative accelerations on particles which coincide with the oscillating flow shown in Fig. 3(c) and the small variations on the pressure field shown in Fig. 3(e).

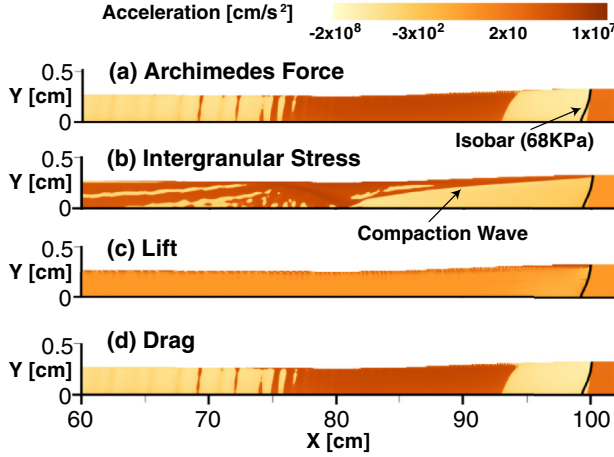


FIG. 5. Particle accelerations in the dust layer, defined as  $\alpha_{s,\text{disp}} > 0.1$ , produced by the vertical component of forces presented in Table I, except gravity. Results normalize pressure gradients, intergranular stresses, and lift and drag forces by  $\alpha_s \rho_s$ . The vertical length scale has been stretched approximately 10 times.

In the dispersed dust, the intergranular stress is related to the solid pressure as  $F_{\text{gran}} = \nabla p_s$ , since  $\alpha_{s,\text{disp}} < 0.1$  and  $p_{\text{fric}} = 0$  in Eq. (12). The solid pressure, in turn, is a function of the particle concentration, as seen in the equation of state of the granular gas [Eq. (9)]. Therefore, the intergranular stress is a function of the particle concentration gradient. This dependency is observed in Fig. 4(b), where the larger accelerations produced by  $F_{\text{gran}}$  correspond to the regions where the larger gradients of particle concentration occur: the top and the bottom of the dispersed dust. In the remainder of the dispersed region, the effect of intergranular stress is weak, except for the narrow regions observed between 40 and 55 cm, where flow oscillations and turbulence produce significant variations on the particle concentration field.

In this investigation, the aerodynamic lift is modeled by the Magnus force, which results from the interaction of the particles with a rotational flow and of the velocity difference between particles and gas [Eq. (18)]. Figure 4(c) shows that the Magnus force raises particles near the shock, where shearing produces vorticity. Behind this region, the flow oscillations and the development of a boundary-layer-like flow control the magnitude and direction of the lift force. In particular, lift produces large accelerations near the edge of the dispersed dust, where the relative velocity of the gas with respect to the particles is large [see Fig. 3(d)]. Moreover, Fig. 4(d) shows that drag forces accelerate particles downwards near the shock and produce alternating positive and negative accelerations of particles further behind the shock due to the flow oscillations.

To summarize, Fig. 4(e) shows the net acceleration of particles produced by the combination of all forces, including gravity. This figure shows some features that should be noted. First, lift controls the particle acceleration near the shock, whereas drag controls the particles located further behind the shock. Moreover, the net acceleration near the bottom and at the edge of the dispersed dust is positive, which is consistent with the particle acceleration promoted by intergranular stresses. These features provide an idea of the forces controlling the particle dynamics at the different locations of the dispersed dust. This analysis is extended in Sec. IV B 3 by measuring the particle acceleration promoted by the different forces in selected locations behind the shock.

## 2. Particle acceleration in the dust layer

Figure 5 shows the acceleration that the Archimedes force, intergranular stress, lift, and drag forces produce on particles within the dust layer for the first 40 cm behind the shock. These graphs show that Archimedes and drag forces accelerate particles downwards near the shock. Then, in

the region between approximately 75 and 93 cm, they accelerate particles upwards. In the region behind 75 cm, Archimedes and drag forces again accelerate particles downwards. The contour of intergranular stress allows us to identify a compaction wave. The figure also shows that the effect of the lift force is negligible throughout this region.

Figure 5(a) shows that the Archimedes force accelerates particles downward between 93 and 100 cm as a result of the pressure gradient forming immediately behind the shock [see Fig. 3(e)]. The particles moving down compact the dust layer, increasing the pressure in the region between 78 and 95 cm. This high-pressure region [also seen in Fig. 3(e)] opposes the compaction of the dust and changes the sign of the particle acceleration driven by the Archimedes force from negative to positive.

Figure 5(b) shows the effect of the compaction wave on the particle acceleration. Note in particular that the compaction wave produces a transition from negative to positive acceleration between 82 and 100 cm. The compaction wave reflects from the floor of the channel around 82 cm. The reflected wave reaches the surface of the dust layer at 75 cm, producing acoustic waves which enhance the flow oscillations seen in Fig. 3(c) [10].

Since the gas flowing through the dust layer is much slower than the flow in the dispersed dust, the effect of the lift force on the dust layer is negligible [Fig. 5(c)]. Drag forces driven by gas flowing downwards, however, initiate the dust compaction between 95 and 100 cm [Fig. 5(d)]. The pressurization of the gas between 75 and 93 cm turns the gas flow upwards, resulting in a positive value of the drag force in this region.

### 3. Variation of forces with distance from the shock

We now examine how the forces that control particle dynamics change with distance from the shock front. Specifically, Fig. 6 shows the particle acceleration produced by the Archimedes force, intergranular stress, lift, and drag along vertical lines located 2, 10, 20, and 30 cm behind the shock. These locations are indicated in the net acceleration contour on top of the figure by lines A, B, C, and D, respectively. The results include dashed lines to indicate the height of the dust layer at every location.

In line A, located 2 cm behind the shock, the lift and intergranular stress raise particles located in the dispersed-dust region, overcoming drag. The lift force produces a much larger particle acceleration than the drag force. The net acceleration indicates that almost all the dispersed particles accelerate upwards in this location. The results in the dust layer, located below the dashed line, show that drag and Archimedes forces accelerate particles downwards, initiating the compaction of the dust layer.

In line B, located 10 cm behind the shock, the peak acceleration driven by lift has reduced with respect to location A; the intergranular stress causes larger accelerations than it does in location A, and drag does not oppose the rise of particles but increases it. The net acceleration of the particles dispersed in location B is positive and larger than in location A. However, only the upper half of the dispersed region experiences a large upward acceleration. The dust layer, in turn, shrinks as a result of the dust compaction initiated near the shock, although drag and Archimedes forces oppose the compaction of the dust in this location.

In line C, which is 20 cm behind the shock front, the dispersed region is higher than in lines A and B. Here, intergranular forces keep lifting particles near the edge of the dispersed dust, and the effect of the aerodynamic lift force is weaker than near to the shock. Drag accelerates the particles upwards, although this acceleration corresponds to a local value which is followed by a downward acceleration [see the alternating positive and negative accelerations in Fig. 4(d)]. A major difference with respect to the previous A and B locations is that the intergranular stress also raises particles located at the bottom of the dispersed region. In the dust layer, the effect of drag and Archimedes forces is weaker than it is in location B. Here, intergranular forces produce a large acceleration near the channel floor as a result of the reflection of the compaction wave, which occurs near this location.

Further behind the shock, in line D, the effect of the multiple forces is considerably lower than in locations A, B, and C. Here, the height of the dispersed region is much larger than in line A.

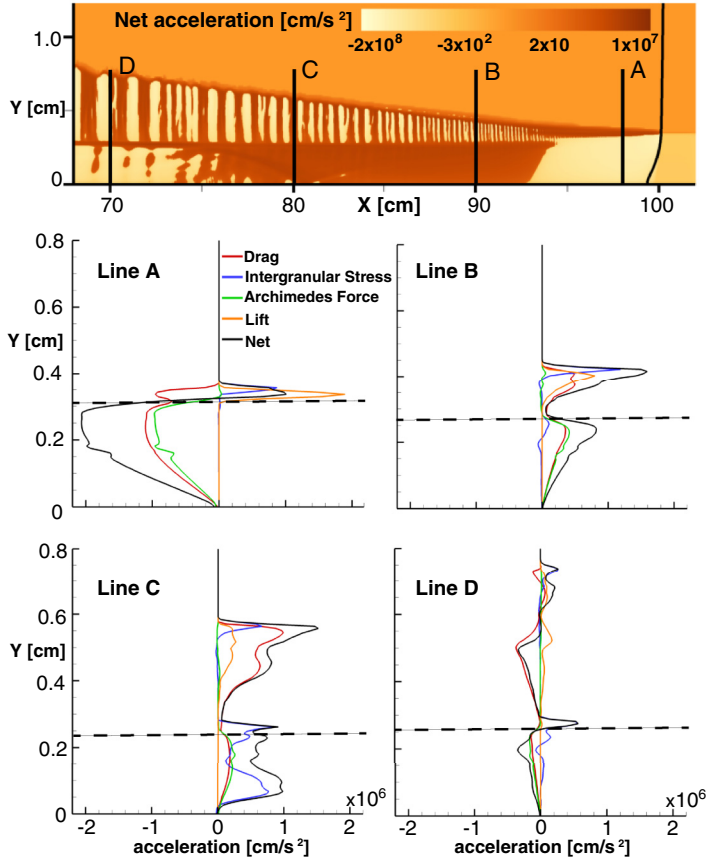


FIG. 6. Particle accelerations driven by drag, intergranular stress, Archimedes force, and lift calculated along the four vertical lines indicated in the net acceleration contour on top. Dashed lines identify local dust-layer height. Shock is at  $X_{\text{shock}} = 100$  cm.

The drag force controls the motion of the dispersed particles, producing downward accelerations. Moreover, it is interesting to see that the height of the dust layer is slightly larger than in location C, indicating the reversal of the dust compaction initiated near the shock.

Results in Fig. 6 show that the dispersed particles are controlled by lift forces near the shock and by drag forces further behind the shock, and that intergranular forces act at the edge and at the bottom of the dispersed dust, confirming the observations made in Sec. IV B 1. In the dust layer, Archimedes and drag forces control the particle motion, which is also modified by intergranular forces resulting from the reflection of the compaction wave.

## V. DISCUSSION

### A. What initiates the dispersion of particles?

To address this question, we focus on particles at the edge of the dispersed region, because these particles were at the edge of the dust layer before the passage of the shock. Therefore, the dispersion must start with these particles. The edge of the dispersed dust is defined as  $\alpha_{s,\text{edge}} = 5 \times 10^{-4}$ .

The components of the particle acceleration at the edge, as seen in Fig. 7, show that the intergranular stress is the major driver of particle dispersion. In fact, without intergranular forces, drag would overcome lift, thereby lowering the dispersed dust. Figure 6 showed that, near the

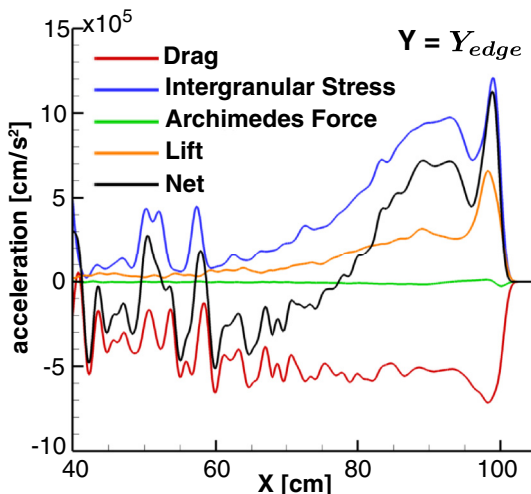


FIG. 7. Particle acceleration driven by drag, intergranular stress, Archimedes force, and lift, calculated at the edge of the dispersed-dust region. Shock is at 100 cm.

shock, lift produces larger accelerations on the dispersed dust than intergranular forces. However, intergranular forces determine the gradient of solid pressure ( $p_s$ ) that initiates the particle dispersion. Specifically, the passage of the shock increases the granular energy of particles, which increases the solid pressure in the dust [see Eqs. (8) and (9)]. As a result, a large gradient of  $p_s$  forms at the surface of the dust, since it is beneath a region without particles (where  $p_s = 0$ ). This solid pressure gradient at the dust surface initiates the particle dispersion.

Aerodynamic lift acts on already dispersed particles, especially those near the shock. As the shock propagates downstream, the particle dispersion at the edge of the dispersed region (that is, bordering on the pure gas) is enhanced by intergranular forces, and these further disperse the dust. Drag forces oppose the rising of particles along the edge of the dispersed region. The net acceleration of particles in Fig. 7 shows drag overcomes the combined effect of intergranular stress and lift at  $\sim 80$  cm. Therefore, the most particle dispersion occurs between  $\sim 80$  cm and the shock front.

### B. Particle and gas dynamics in the dust layer

The deflection of the gas flow and the pressure gradient in the dust allow the gas to penetrate the dust layer, which is an effect similar to what occurs in Darcy flow through porous media. The evolution of this flow and its effect on the particles is shown in Fig. 8, where the pressure, gas, and particle velocities are computed along a horizontal line located in the dust layer, 0.2 cm above the channel floor.

Figure 8 shows that a downward gas flow begins immediately behind the shock and pushes the particles down with it. As dust is compressed, the pressure in the dust layer rises and the gas slows down, as seen in the region between 93 and 100 cm. A further increase in the gas pressure turns the gas flow upwards between 75 and 93 cm, and therefore works against the compaction process. At locations lower than 75 cm, the particles also move upwards, expanding the dust layer. These changes in the gas and particle motion determine the changes in the sign of the acceleration driven by Archimedes and drag forces, as shown in Figs. 5(a) and 5(d), respectively.

### C. Particle acceleration further away from the shock

Earlier in this paper, we identified the mechanisms controlling the particle dynamics in the region extending up to 60 cm behind the shock. The results showed that the most important changes in the

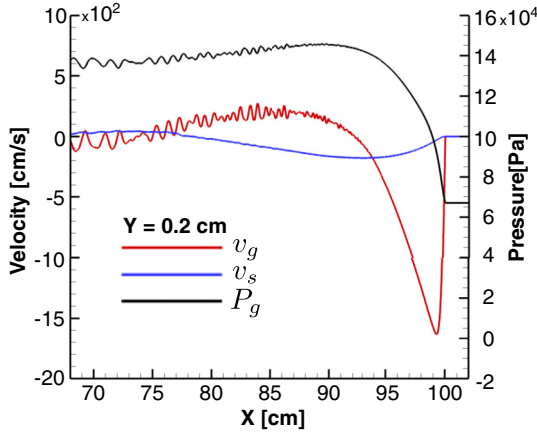


FIG. 8. Gas pressure and vertical component of the gas and particle velocities computed along a horizontal line located in the dust layer, 0.2 cm above the channel floor. Shock is located at 100 cm.

particle dynamics occur near the shock front (for instance, see how the forces computed 2 cm behind the shock decay 30 cm behind the shock in Fig. 6). In Fig. 9, we have extended the region of interest to 200 cm behind the shock front. Figure 9 are profiles of the forces at two locations: a horizontal line in the dust layer, located 0.2 cm above the floor of the channel [Fig. 9(a)], and the edge of the dispersed dust, which is defined as in Sec. V A as  $\alpha_{s,\text{edge}} = 5 \times 10^{-4}$  [Figs. 9(b)–9(d)].

Figure 9(a) shows that the major effects of the forces on the dust layer occur in the first 50 cm after the shock passes. Further upstream than 50 cm, there are no significant forces acting on the dust particles in the dust layer. The situation is similar in the dispersed dust [Fig. 9(b)], where drag, lift, and Archimedes forces do not modify the particle dynamics significantly beyond 230–240 cm. Only the intergranular stress continues to accelerate particles beyond this point. The particle acceleration produced by intergranular forces beyond 230–240 cm, however, shows large oscillations, and the resulting net acceleration is less than the net acceleration produced near the shock.

These results indicate that, for the conditions listed in Table II, the region extending approximately 60–70 cm behind the shock controls the particle rising. This conclusion is also seen in Fig. 9(c), where the height of the dispersed dust shows that the particles rise quickly within the first 60 cm behind the shock. The height of the dispersed dust decays between 210 and 240 cm and then oscillates with no significant change in the net height. This is explained by looking at the forces in Fig. 9(b) and the height of the dispersed particles in Fig. 9(c). For example, the decay between 210 and 240 cm in Fig. 9(c) is the result of forces applied earlier on the particles, between 250 and 270 cm, which overcome the particle rising initiated near the shock.

The acceleration rates in Fig. 9(b) are similar to those obtained in Fig. 7, even though Fig. 7 corresponds to a case where the shock has propagated 100 cm and Fig. 9(b) to a case where the shock has propagated 300 cm. Therefore, the particle dynamics behind the shock is a quasisteady process. This conclusion is reinforced by the results of Fig. 9(d), which overlaps the heights of the dispersed dust corresponding to multiple shock propagation distances. The overlapped results show that all of the cases have a similar lifting rate at the beginning, before the forces begin oscillating at around 60 cm behind the shock.

#### D. Effect of model parameters on particle dynamics

As discussed above, the particle dispersion is initiated by a gradient of solid pressure that occurs at the dust surface, after the passage of the shock. The solid pressure is determined by particle collisions in a way similar to the way molecular collisions determine gas pressure. Therefore, the characteristics of the particle collisions (whether elastic or inelastic collisions) modify the

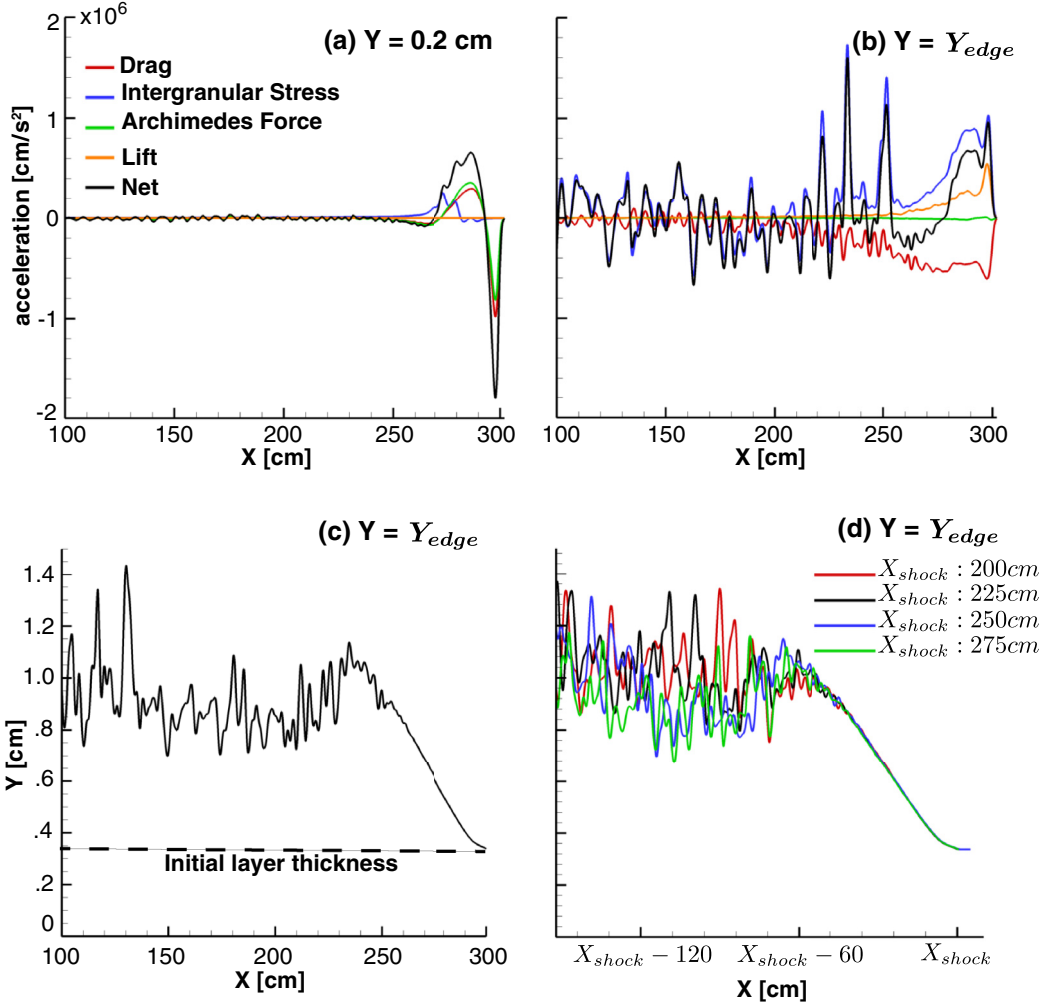


FIG. 9. Particle acceleration driven by drag, intergranular stress, Archimedes force, and lift, calculated in the dust layer (a) and at the edge of the dispersed particle cloud (b). Edge of dispersed-dust region (c) corresponding to  $X_{shock} = 300$  cm and to multiple locations of the shock (d).

solid pressure and, consequently, the initiation of the particle dispersion. In our physical model, the coefficient of restitution  $e$  in Eq. (9) determines the elasticity of particle collisions. In this investigation, we consider particle collisions that are essentially elastic ( $e = 0.9$ ). Lower values of the coefficient of restitution would lead to smaller gradients of the solid pressure and, as a result, a delay in the dispersion of particles.

Another important parameter in our physical model is the lift coefficient  $C_l$  in the Magnus force [Eq. (18)]. The Magnus force is a function of the velocity difference between gas and particles, and of the velocity gradients in the gas flow. The passage of the shock produces a boundary layer in the gas phase, which is very thin in the region immediately behind the shock. As a result, extremely large velocity gradients develop in this region that complicate the computation of lift. Lifting force models for dust layers were developed using incompressible flow theory and almost certainly need modification for high-speed, compressible flows. The lift coefficient could be defined in such a way that it accounts for the sharp change of the gas velocity at the shock. Determining a better  $C_l$  for this shock problem, however, is a challenging research problem which we leave for future work.

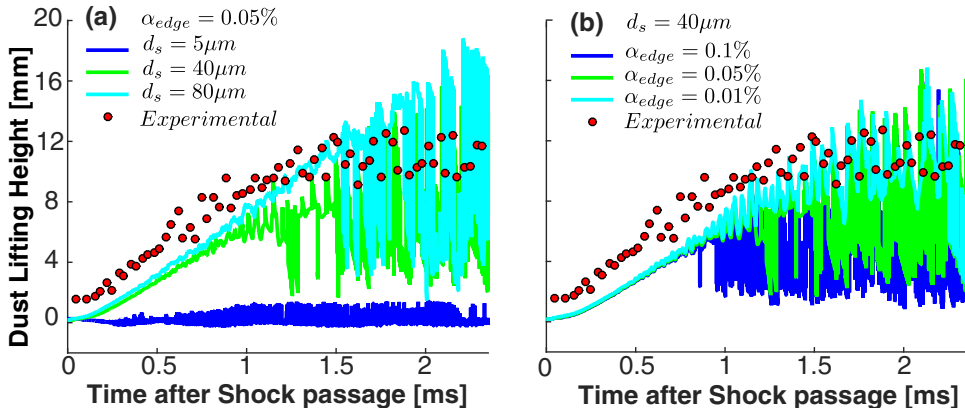


FIG. 10. Dust-cloud height as a function of time after shock passage obtained experimentally and numerically. Multiple case simulations vary with particle size (a) and definition of the edge of the dispersed region (b).

### E. Comparison with experiments

The results of the simulations have been compared to the experimental shock-tube results of Chowdhury *et al.* [4]. Their experimental setup consisted of a stainless steel shock tube in which the driven section is  $10.8 \times 10.8 \text{ cm}^2$  and 4.1 m long. Inside the shock tube, there was a pan with limestone dust at the bottom. The experiments considered two heights of the dust layer,  $h_d = 0.32$  and 1.27 cm, where the dust was dispersed by shock waves with  $M_s = 1.1, 1.23, 1.32, 1.4,$  and 1.6. The remaining operating conditions are similar to those listed in Table II. They reported an average size of the dust particles of  $d_{s,\text{exp}} = 4.2 \text{ }\mu\text{m}$ . Images from scanning electron microscopy (SEM) of the particles, however, indicate that the effective size of the particles was significantly larger than this value. The analysis of these images was further examined in a recent publication [26], where SEM images showed agglomeration to sizes of 50–175  $\mu\text{m}$ .

Particle agglomeration is more likely when the particles approach the micro- and nanoscales, given that the surface forces (such as electrostatic and van der Waals forces) become comparable to the volumetric forces in these length scales. In fact, the air fluidization of limestone particles with an average size of 4.2  $\mu\text{m}$  corresponds to Group C in Geldart’s classification of fluidized particle-bed behavior [27]. One characteristic of Group C is that large cohesive forces develop and make fluidization of particles difficult. Therefore, the particle diameter that should be used to compare the computations to experiments for this dust-lifting problem becomes a value to be determined instead of an input quantity.

Figure 10(a) compares numerical and experimental results for  $M_s = 1.4$ . The computational results are for three simulations, each with a different, constant particle diameter of  $d_s = 5, 40,$  or 80  $\mu\text{m}$ . The results corresponding to 5  $\mu\text{m}$  do not agree well with the experimental data. For this particle size, the inertial forces of the particles are much smaller than the drag forces produced by the fluid motion. As a result, the particles do not rise but instead follow the boundary-layer motion of the gas flow. Simulations of 40- and 80- $\mu\text{m}$  particles, however, reproduce the initial, quasilinear growth of particle lifting reported in Ref. [4]. Simulations of 40- $\mu\text{m}$  particles reproduce, in addition, the second stage reported in Ref. [4], where the height of dust-lifting plateaus after approximately 1.5 ms.

Chowdhury *et al.* [4] define the edge of the dispersed dust based on red-blue-green pixel values from a high-speed camera. This is difficult to implement in the numerical simulations, which instead use a threshold value of the solid volume fraction,  $\alpha_{s,\text{edge}}$ , to define the edge of the dispersed dust. Based on the optical thickness of the particles dispersed experimentally, the range of  $\alpha_{s,\text{edge}}$  should be 0.01–0.1%. The effect of  $\alpha_{s,\text{edge}}$  on the comparison of numerical and experimental results is

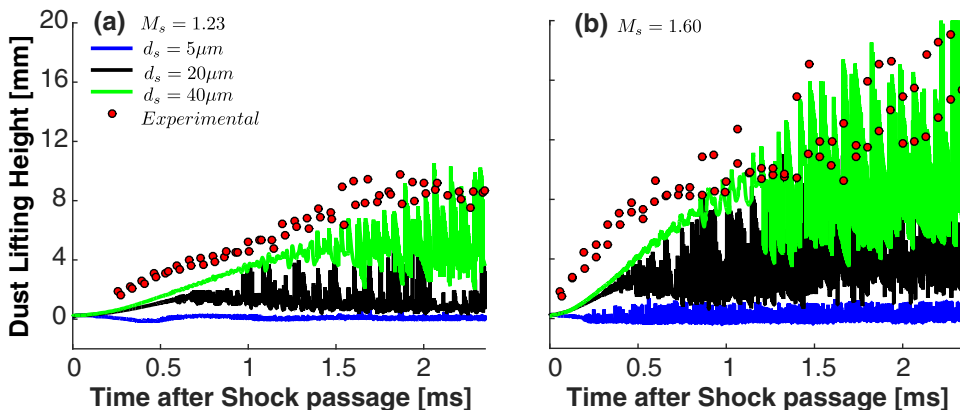


FIG. 11. Dust-cloud height as a function of time after shock passage obtained experimentally and numerically. Multiple case simulations vary with particle size.

shown in Fig. 10(b), for particle diameter  $d_s = 40 \mu\text{m}$ . In these results, the value used in the previous sections,  $\alpha_{s,\text{edge}} = 0.05\%$ , is the one that better reproduces the rise and plateau of particles obtained experimentally. The difference in the computational and experimental definitions of  $\alpha_{\text{edge}}$  may cause the shift between the numerical results and the experimental data at  $t = 0$ .

The comparison of numerical and experimental results is complemented with the  $M_s = 1.23$  and 1.6 cases in Fig. 11. As in Figure 10(a), simulations of 40- $\mu\text{m}$  particles agree well qualitatively with the experimental data. The two-dimensional nature of the simulations leads to larger oscillations than the experimental results, but the initial rise and subsequent plateau of the dispersed particles are reproduced.

## VI. SUMMARY AND CONCLUSIONS

A two-fluid model is used to investigate the dispersion of particles from a shock wave moving along and through a thin layer of dust (as shown in Fig. 1). Specifically, we simulate the propagation of a Mach-1.4 shock moving through a layer of limestone dust consisting of particles of diameter 40  $\mu\text{m}$ . The initial layer thickness and dust volume fraction in the dust layer are 0.32 cm and 0.47%, respectively.

The numerical model used here solved multidimensional, unsteady coupled sets of fluid equations for a compressible gas and a granular fluid which consists of a mixture of solid particles and gas. The particle dynamics in and above the dust layer are computed by analyzing the vertical component of the forces experienced by the particles as a result of the passage of the shock. These forces are the Archimedes force produced by gas pressure gradients, drag and lift forces produced by the relative motion between particles and gas, intergranular forces resulting from particle collisions and frictional stress, and the gravitational force.

The first interaction of the shock with the dust layer produces two major changes in the shock structure. First, the shock front curves as it enters the dust layer, and this deflects the gas flow downwards. Second, the shock weakens inside the dust, becoming a compression wave. As the shock wave propagates through the dust layer, two regions form behind the shock: a compacted dust layer and a dispersed-dust region.

Aerodynamic drag forces, produced by the deflected gas flow, and the Archimedes force, produced by the compression wave inside the dust, compact the particles in the layer. This compaction evolves to a compaction wave, which increases the intergranular stress on particles inside the layer. Particle dispersion is initiated by intergranular forces immediately after the shock passes. After this, the

particle dispersion is produced by lift and intergranular forces, and opposed by drag. The effect of lift weakens with distance from the shock.

Thus, we see the importance of the initial interaction of the shock and the dust layer in creating the conditions for dispersion, which occurs primarily in a fixed region behind the shock front. For the specific conditions in this calculation, as given by the parameters in Table II, particle dispersion is controlled by the forces acting in the first 50–60 cm behind the shock front.

The results of the simulations were compared to preexisting experimental measurements made by Chowdhury *et al.* [4]. Particle agglomeration, which results in fluidized layers of particles, made it difficult to determine the particle size in the experiments. The initial experimental particle size was supposed to be 4.2  $\mu\text{m}$ . SEM (scanning electron microscope) measurements showed, however, that the particles were much larger. Thus the experimental data after the shock passed was compared to simulations of 5-, 20-, 40-, and 80- $\mu\text{m}$  particles. The simulations for 40- $\mu\text{m}$  particles were in both quantitative and qualitative agreement with the measured initial growth of particle lifting and the plateau of the dust-lifting height for the cases  $M_s = 1.23, 1.4, \text{ and } 1.6$ .

Future work will involve simulations to examine how the forces acting on the particles vary with particle size, the effect of the height of the dust layer, and the effects of multiple particles sizes and types. In addition, a study of the effects of the choice of specific input parameters, such as the coefficient of restitution and the lift coefficient, must be evaluated.

#### ACKNOWLEDGMENTS

We thank Mike Sapko and Marcia Harris for their thoughtful questions and input. This work was supported in part by NIOSH Grant No. 200-2015-64091 and in part by the University of Maryland through Minta Martin Endowment Funds in the Department of Aerospace Engineering, and through the Glenn L. Martin Institute Chaired Professorship at the A. James Clark School of Engineering. The authors acknowledge the University of Maryland supercomputing resources (<http://www.it.umd.edu/hpcc>), made available in conducting the research reported in this paper.

- 
- [1] M. Sichel, C. W. Kauffman, and Y. C. Li, Transition from deflagration to detonation in layered dust explosions, *Process Saf. Prog.* **14**, 257 (1995).
  - [2] J. H. Gerrard, An experimental investigation of the initial stages of the dispersion of dust by shock waves, *Br. J. Appl. Phys.* **14**, 186 (1963).
  - [3] R. Klemens, P. Zydak, M. Kaluzny, D. Litwin, and P. Wolanski, Dynamics of dust dispersion from the layer behind the propagating shock wave, *J. Loss Prev. Process Ind.* **19**, 200 (2006).
  - [4] A. Y. Chowdhury, H. G. Johnston, B. Marks, M. S. Mannan, and E. L. Petersen, Effect of shock strength on dust entrainment behind a moving shock wave, *J. Loss Prev. Process Ind.* **36**, 203 (2015).
  - [5] R. K. Eckhoff, *Dust Explosions in the Process Industries* (Elsevier, New York, 2003).
  - [6] R. W. Houim and E. S. Oran, Numerical simulation of dilute and dense layered coal-dust explosions, *Proc. Combust. Inst.* **35**, 2083 (2015).
  - [7] R. W. Houim and E. S. Oran, A multiphase model for compressible granular-gaseous flows: Formulation and initial tests, *J. Fluid Mech.* **789**, 166 (2016).
  - [8] D. Gidaspow, *Multiphase Flow and Fluidization* (Academic Press, New York, 1994).
  - [9] B. Fletcher, The interaction of a shock with a dust deposit, *J. Phys. D: Appl. Phys.* **9**, 197 (1976).
  - [10] R. W. Houim, O. J. Ugarte, S. Lai, and E. S. Oran, Mechanisms of dust scouring behind shock waves, in *Proceedings of the 11th International Symposium on Hazards, Prevention, and Mitigation of Industrial Explosions* (Dalian University of Technology Electronic & Audio-visual Press, Dalian, China, 2016), pp. 188–202.

- [11] C. C. Hwang, Initial stages of the interaction of a shock wave with a dust deposit, *Int. J. Multiphase Flow* **12**, 655 (1986).
- [12] T. Suzuki and T. Adachi, The effects of particle size on shock wave-dust deposit interaction, in *Proceedings of the 14th International Symposium on Space Technology and Science* (AGNE Publishing, Inc, Tokyo, Japan, 1984), pp. 483–490.
- [13] A. V. Fedorov and I. A. Fedorchenko, Computation of dust lifting behind a shock wave sliding along the layer, Verification of the model, *Combust., Explos. Shock Waves (Engl. Transl.)* **41**, 336 (2005).
- [14] B. E. Gelfand, S. P. Medvedev, A. A. Borisov, A. N. Polenov, S. M. Frolov, and S. A. Tsyganov, Shock loading of stratified dusty systems, *Combustion* **9**, 153 (1989).
- [15] P. Zydak and R. Klemens, Modelling of dust lifting process behind propagating shock wave, *J. Loss Prev. Process Ind.* **20**, 417 (2007).
- [16] K. Balakrishnan, D. V. Nance, and S. Menon, Simulation of impulsive effects from explosive charges containing metal particles, *Shock Waves* **20**, 217 (2010).
- [17] R. W. Houim and E. S. Oran, Structure and flame speed of dilute and dense layered coal-dust explosions, *J. Loss Prev. Process Ind.* **36**, 214 (1987).
- [18] P. C. Johnson and R. Jackson, Frictional-collisional constitutive relations for granular materials, with application to plane shearing, *J. Fluid Mech.* **176**, 67 (1987).
- [19] D. A. Drew and R. T. Lahey, Jr., The virtual mass and lift force on a sphere in rotating and straining inviscid flow, *Int. J. Multiphase Flow* **13**, 113 (1987).
- [20] D. J. Gunn, Transfer of heat of mass to particles in fixed and fluidized beds, *Int. J. Heat Mass Transfer* **21**, 467 (1978).
- [21] D. L. Koch and A. S. Sangani, Particle pressure and marginal stability limits for a homogenous monodisperse gas fluidized bed: Kinetic theory and numerical simulations, *J. Fluid Mech.* **400**, 229 (1999).
- [22] C. K. K. Lun, S. B. Savage, D. J. Jeffrey, and N. Chepurnyi, Kinetic theories for granular flow: Inelastic particles in Couette flow and slightly inelastic particles in a general flowfield, *J. Fluid Mech.* **140**, 223 (1984).
- [23] R. J. Spiteri and S. J. Ruuth, A new class of optimal high-order strong-stability-preserving time discretization methods, *SIAM J. Numer. Anal.* **40**, 469 (2003).
- [24] P. MacNeice, K. M. Olson, C. Mobarry, R. de Fainchtein, and C. Packer, PARAMESH: A parallel adaptive mesh refinement community toolkit, *Comput. Phys. Commun.* **126**, 330 (2000).
- [25] A. Y. Chowdhury, B. D. Marks, H. G. Johnston, M. S. Mannan, and E. L. Petersen, A new facility for studying shock-wave passage over dust layers, *Shock Waves* **26**, 129 (2016).
- [26] H. G. Johnston, A. J. Chowdhury, M. S. Mannan, and E. L. Petersen, Effect of coal-limestone mixtures on dust dispersion behind a moving shock wave, *J. Loss Prev. Process Industries* **44**, 551 (2016).
- [27] D. Geldart, Types of gas fluidization, *Powder Technol.* **7**, 285 (1973).